



Towards possible opportunities in nuclear materials science and technology at an X-ray free electron laser research facility

A. Froideval^{a,*}, A. Badillo^a, J. Bertsch^a, S. Churakov^a, R. Dähn^a, C. Degueldre^a, T. Lind^a, D. Paladino^a, B.D. Patterson^b

^a Nuclear Energy and Safety (NES), Paul Scherrer Institute, CH-5232 Villigen PSI, Switzerland

^b SwissFEL Project, Paul Scherrer Institute, CH-5232 Villigen PSI, Switzerland

ARTICLE INFO

Article history:

Available online 12 February 2011

ABSTRACT

Spectroscopy and imaging of condensed matter have benefited greatly from the availability of intense X-ray beams from synchrotron sources, both in terms of spatial resolution and of elemental specificity. The advent of the X-ray free electron laser (X-ray FEL) provides the additional features of ultra-short pulses and high transverse coherence, which greatly expand possibilities to study dynamic processes and to image non-crystalline materials. The proposed SwissFEL facility at the Paul Scherrer Institute is one of at present four X-ray FEL projects worldwide and is scheduled to go into operation in the year 2017. This article describes a selection of problems in nuclear materials science and technology that would directly benefit from this and similar X-ray FEL sources. X-ray FEL-based experiments are proposed to be conducted on nuclear energy-related materials using single-shot X-ray spectroscopy, coherent X-ray scattering and/or X-ray photon correlation spectroscopy in order to address relevant scientific questions such as the evolution in time of the irradiation-induced damage processes, the deformation processes in nuclear materials, the ion diffusion processes in the barrier systems of geological repositories, the boiling heat transfer in nuclear reactors, as well as the structural characterization of graphite dust in advanced nuclear reactors and clay colloid aggregates in the groundwater near a radioactive waste repository.

© 2011 Elsevier B.V. All rights reserved.

1. Introduction

The approximately 10 order-of-magnitude relative increase in peak brightness from a dental X-ray machine to a 3rd generation synchrotron is similar to that from the synchrotron to a X-ray free electron laser (X-ray FEL). A representative X-ray FEL, the SwissFEL project at the Paul Scherrer Institute, will produce 20-fs pulses of X-rays in the wavelength range 0.1–7 nm, each of which consists of 10^{11} photons, i.e. the fluence available in approximately a second at a synchrotron beamline. And as expected of a laser source, the X-ray FEL radiation will be fully spatially coherent.

This qualitative jump in source performance opens up new experimental methods and scientific applications. Of ever increasing importance in the field of nuclear materials science and technology are numerical simulations of structure and dynamics at or close to the atomic-scale. Key investigations with the X-ray FEL facilities will plausibly have the greatest impact in this field by providing stringent tests of the methods and of the parameters used in simulations. In this article, we present selected examples of such

investigations, which are of great current importance to nuclear materials scientists and which are well-suited to the capabilities of the planned SwissFEL facility.

In a “pump–probe” experiment, an optical laser or other pulsed source is used to perturb the sample, and a synchronized X-ray FEL pulse is used to probe its reaction. With repeated measurements at different time delays, a time-resolved picture of the dynamic evolution is obtained. We propose two examples of pump–probe experiments at the SwissFEL, which use coherent X-ray scattering to statistically characterize the perturbed sample at the micro- or nano-scale. The first is a test of nucleate boiling heat transfer models, in which local superheating of a liquid layer by an intense optical laser pulse is followed by a coherent scattering snapshot of the resulting mixed liquid–vapor state. The second is a statistical study of the development of vacancy and interstitial clusters and of crack initiation and propagation in e.g. reactor pressure vessel steels, using diffuse X-ray scattering following defect initiation by high-energy particle-ion implantation or by laser-induced shock waves.

With the X-ray Photon Correlation Spectroscopy technique, the X-ray FEL also offers the opportunity to measure time- and wave-vector-dependent atomic-scale correlations at equilibrium, without the requirement of a pump pulse. The resulting intermediate

* Corresponding author. Tel.: +41 56 310 44 48.

E-mail address: annick.froideval@psi.ch (A. Froideval).

scattering function $S(q, \tau)$ can provide a sensitive test of, for example, the interlayer diffusion parameters for heavy ions in the clay minerals of a radioactive waste depository. Finally, the single-shot coherent scattering of *resonant* X-rays can be used to test models of the chemical structure of air- and water-borne nanoparticles either emanating from a nuclear reactor or carrying radionuclides.

The article is organized as follows: in Section 2, the operation principle of a X-ray FEL is briefly explained, the specifications of the four X-ray FEL projects worldwide are summarized, with emphasis on those of the SwissFEL, and several pertinent X-ray FEL measurement techniques are described. Section 3 gives details of four X-ray FEL-based tests of simulation model parameters, which we feel are of particular interest to nuclear energy-related materials. The conclusions are presented in Section 4.

2. Instrumentation and methods

2.1. Principle of operation of an X-ray FEL

The main components of an X-ray FEL are shown in Fig. 1a. As in a synchrotron, an accelerator produces bunches of relativistic electrons which follow a “wiggling” trajectory in a magnetic undulator, radiating pulses of spontaneous X-radiation. In contrast to a synchrotron, however, a linear accelerator is used in the X-ray FEL, and instead of several meters, the undulator has an overall length of many tens of meters. The high beam quality and long undulator cause the electron bunches to self-organize into “micro-bunches” (see Fig. 1b), leading to a coherent amplification to saturation via the self-amplifying spontaneous emission (SASE) process [1].

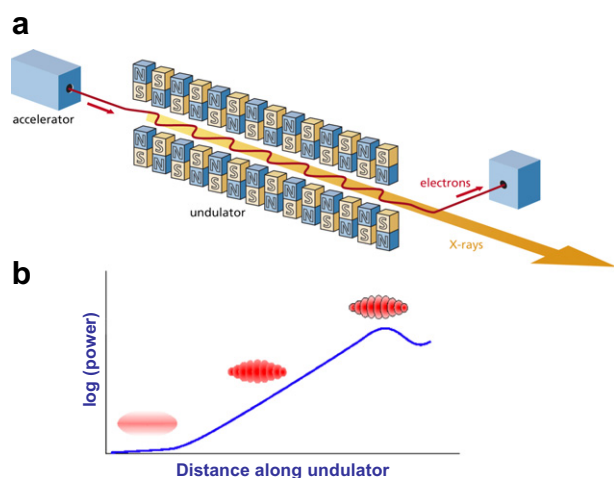


Fig. 1. (a) Schematic view of the main components of an X-ray FEL and (b) graphical representation of the SASE effect, showing the development of “micro-bunching” of the electron pulse and the exponential increase in photon flux [2].

2.2. The SwissFEL and other X-ray FEL facilities worldwide

There are currently four X-ray FEL projects with the goal of producing hard X-rays (X-ray wavelength $\lambda \approx 0.1$ nm), and their specifications are presented in Table 1. The Linac Coherent Light Source (LCLS) [3] in the United States produced first coherent X-rays in April, 2009, and presently under construction are the European XFEL in Germany [4] and the Spring-8 Compact SASE Source (SCSS) in Japan [5]. A further X-ray FEL facility, the SwissFEL, is proposed to be operational in 2017 at the Paul Scherrer Institute, in Würenlingen/Villigen, Switzerland [2,6]. As can be seen from Table 1, the performances of the four projects are quite similar. The SwissFEL has the lowest electron beam energy, permitting a relatively compact overall length of 700 m, but also somewhat reduced peak brilliance. The major difference among the planned X-ray FELs is the high overall repetition rate of the European XFEL (10 pulse trains per second, each containing 3250 micropulses), which is made possible through the use of superconducting accelerator technology. Other generic specifications of the XFEL radiation are: an unfocused beam spot of approximately 200 μm , which can be focused to approximately 100 nm, a relative spectral bandwidth in SASE operation of 10^{-3} , a pulse energy of the order of a mJ, and a peak X-ray power of tens of GW.

A schematic plan of the SwissFEL facility is shown in Fig. 2. After generation in an electron gun and booster, the electron bunches are compressed in two bunch compressors and accelerated in a three-section linac to a maximum energy of 5.8 GeV. Coherent pulses of radiation are then produced in the hard X-ray undulator “Aramis” and the soft X-ray undulator “Athos” and delivered to the experimental areas. Special features of the SwissFEL design are: minimization of the electron energy required for producing hard X-rays, a constant repetition rate of 100 Hz, variable soft-X-ray polarization, the use of seeding to produce transform-limited X-ray pulses, a synchronized source of terahertz (THz) pump radiation, and a broadband mode of operation with $\Delta E/E = 1.2\%$. As parenthetically indicated in the Fig. 2, options exist to extend the spectral range to both shorter and longer wavelengths. By accelerating double electron bunches and with rapid switching, both Aramis and Athos will be able to operate simultaneously at 100 Hz. Each beamline can be directed with X-ray optics into one of three experimental areas, tentatively designated: “coherent diffraction”, “pump–probe”, and “generic”, for Aramis and “pump–probe imaging and scattering”, “pump–probe spectroscopy” and “inelastic scattering”, for Athos.

2.3. X-ray FEL measurement techniques

2.3.1. Single-shot pump–probe X-ray spectroscopy

A variety of X-ray spectroscopic methods have been developed, including photoelectron spectroscopy (PES), X-ray near-edge absorption spectroscopy (XANES), extended X-ray absorption fine

Table 1
Specifications of the XFEL projects worldwide.

XFEL facility	Electron beam energy (GeV)	Pulse duration (fs)	Pulse repetition rate (Hz)	Wavelength range λ (nm)	Peak brilliance at $\lambda = 0.1$ nm (number of photons $(\text{s}^{-1} \text{mm}^{-2} \text{mrad}^{-2})/0.1\%$ bandwidth)
SwissFEL ^a	5.8	5–20	100	0.1–7.0	$\sim 0.5 \times 10^{33}$
European XFEL ^b	17.5	100	10	0.1–6.4	$\sim 5.0 \times 10^{33}$
LCLS ^c	4.5–14.3	10–230	120	0.15–160	$\sim 0.06\text{--}0.8 \times 10^{33}$
SCSS ^d	8.0	500	60	0.1–60	$\sim 0.5 \times 10^{33}$

The European XFEL will produce 3250 micropulses per macropulse at 10 Hz.

^a Ref. [2].

^b Ref. [4].

^c Ref. [3].

^d Ref. [5].

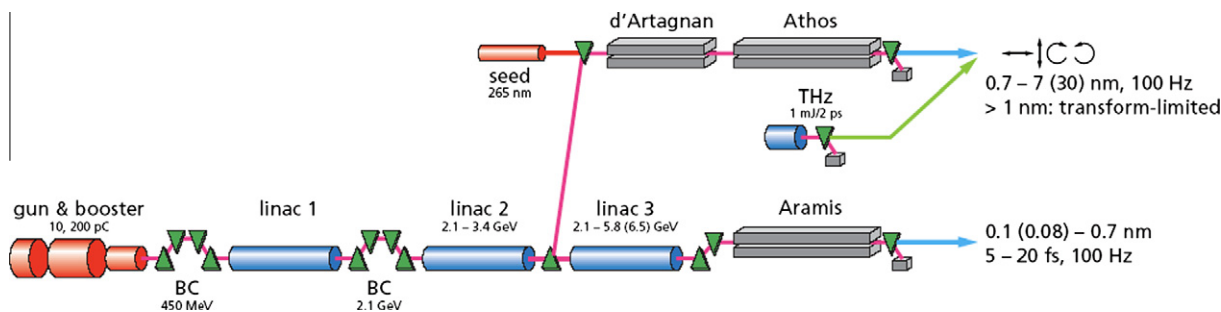


Fig. 2. Schematic overview of the planned SwissFEL machine [6] showing the main components: electron gun and booster, three-stage linear accelerator (linac), bunch compressors (BC), and two undulator beamlines, Aramis and Athos. An independent source of terahertz pump pulses (THz) is also included.

structure (EXAFS), X-ray emission spectroscopy (XES) and resonant inelastic X-ray spectroscopy (RIXS). Since they either use incident X-rays which are close in energy to a characteristic atomic absorption edge or they detect characteristic X-rays emitted in atomic transitions, they are all element-specific. They are complementary techniques – some probe unoccupied electronic levels and others occupied levels, some are sensitive to the electronic structure and others to the local molecular geometry, and some are restricted to dipole-allowed transitions while others are sensitive to, e.g. *d–d* transitions. An example of the sensitivity of a XANES measurement to the local atomic arrangement is shown in Fig. 3. A large literature exists, e.g. [7–9] describing time-resolved pump–probe adaptations of such spectroscopies, in which a synchronized optical laser pulse is used to initiate an electronic excitation, the reaction to which is probed a variable time delay τ later using X-ray spectroscopy.

Adapting such spectroscopies to pump–probe measurements at the X-ray FEL brings the advantage of high-statistics data at time scales as short as tens of femtoseconds. There are, however two principal difficulties. Firstly, since an X-ray FEL pulse may damage the sample, each measurement will require a fresh sample, entailing liquid jets in vacuum or the translation of homogeneous samples. Secondly, due to the statistical nature of the SASE process, one expects fluctuations in the pulse-to-pulse X-ray fluence of up to 50%. Although such variations can be normalized to the incoming flux, it is preferable to perform a complete spectral measurement in a single-shot. In its broadband mode of operation, the SwissFEL,

combined with suitable energy-dispersive detectors [11–13], will permit such measurements. Of interest to the nuclear materials community are time-resolved measurements of chemical processes, for example those related to *in situ* studies of corrosion [14].

2.3.2. Coherent X-ray scattering

The high coherence of the X-ray FEL radiation implies that scattered radiation from widely separated parts of the sample will interfere, yielding a rich “speckle” pattern (see Fig. 4). Using iterative methods of phase-retrieval [15], the electron density in the sample, projected onto a plane perpendicular to the incident beam, can then be obtained. The achievable spatial resolution d of such a measurement is proportional to the inverse fourth root of the incident X-ray fluence (F_0) [16]. Indeed, by making use of the classical electron radius

$$r_e = \frac{1}{4\pi\epsilon_0} \frac{e^2}{m_e c^2} = 2.818 \times 10^{-15} \text{ m} \quad (1)$$

with e the elementary charge, m_e the electron mass, ϵ_0 the permittivity of vacuum and c the speed of light, and of the complex electron density

$$\rho_e = \frac{2\pi(\delta + i\beta)}{\lambda^2 r_e} \quad (2)$$

(with δ the refractive index and β the absorption index), the spatial resolution limit (d) achievable for a number of incident X-rays per unit area F_0 which scatter P photons into a detector is given by:

$$d = \sqrt[4]{\frac{P}{F_0 r_e^2 \lambda^2 |\rho_e|^2}} = \sqrt[4]{\frac{P \lambda^2}{4\pi^2 F_0 (\delta^2 + \beta^2)}} \quad (3)$$

For 10^{11} hard X-ray photons – with a X-ray energy ($h\nu$) of 12.4 keV (i.e. a X-ray wavelength λ of 1 Å) – from a single SwissFEL shot focused into a $100 \times 100 \text{ nm}^2$ spot, it is then predicted that it will be possible to image different relevant nuclear energy-related materials to a spatial resolution ranging from approximately 2–4 nm (Table 2).

In a further development of this technique, use can be made of the elemental contrast available from resonant X-rays at a characteristic absorption edge [18], and one may envisage further extensions which combine spectroscopic and scattering information.

Several points are worthy of consideration when performing coherent scattering measurements at a X-ray FEL facility. First of all, since a single focused X-ray FEL pulse will destroy the sample due to “Coulomb explosion” following electron emission by primary photoemission and secondary Auger processes [19], it is important that the pulse duration be sufficiently short that the recorded scattering pattern corresponds to the sample before it has time to fly apart (“pre-damage diffraction”). It is believed that the 20-fs pulse duration of the SwissFEL is sufficiently short in this regard. Secondly, although the SASE radiation has a high

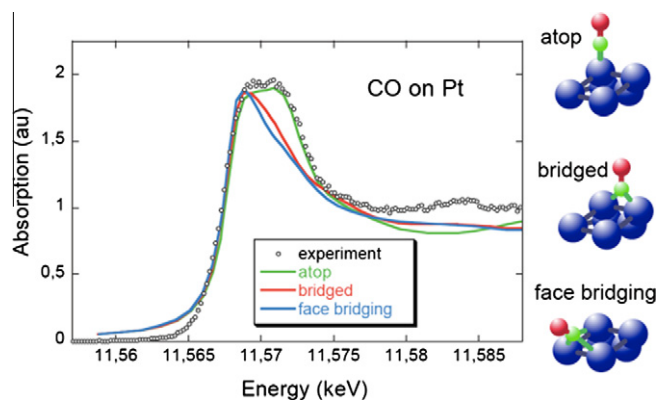


Fig. 3. An example of (static) XANES measurements of 5 wt.% Pt/Al₂O₃, taken at the Pt L₃-absorption edge, which is sensitive to the geometry of chemisorbed CO on Pt/Al₂O₃ [10]. Adapted with permission from [10]. Copyright 2006 American Chemical Society. The spectra represented in red, black and green correspond to partially oxidized Pt particle, uncovered Pt particle, and CO adsorbed dominantly on the atop sites (insert), respectively. With pump–probe experiments at the SwissFEL, such measurements could be performed with single-shots on short-lived intermediate states. (For interpretation of the references to colour in this figure legend, the reader is referred to the web version of this article.)

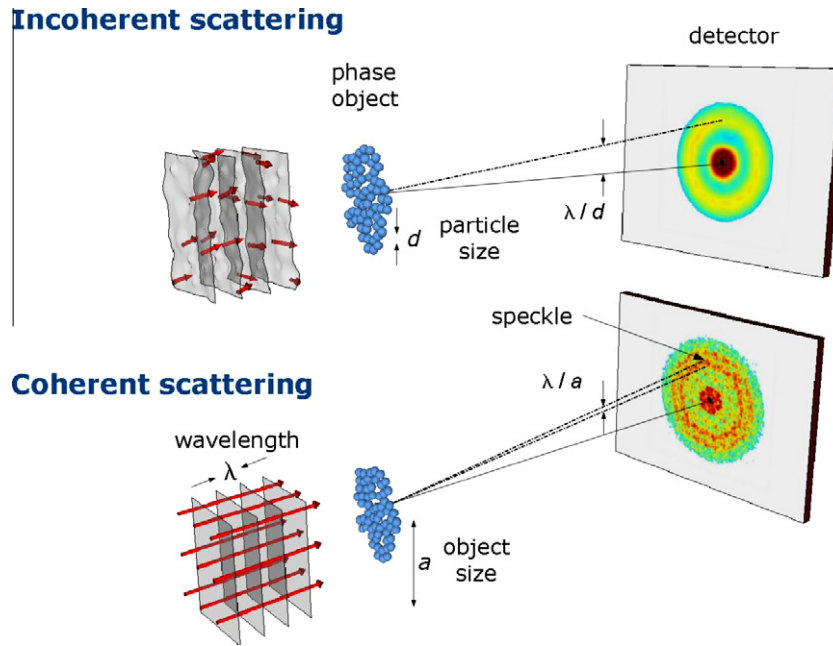


Fig. 4. A comparison of the scattering by a phase object (ignoring absorption) of incoherent and coherent X-rays [15]. From the rich speckle pattern in the coherent case, a detailed 2D-projection of the electron density in the sample can be obtained. Reprinted figure with permission from [15]. Institute of Physics and IOP Publishing Limited 2004.

Table 2

Estimations of the approximate spatial resolution achievable from X-ray scattering experiments conducted on some relevant nuclear energy-related materials. The spatial resolution is calculated from Eq. (3), as described in the text, for the following experimental conditions: $E_{\text{photon}} = 12.4$ keV, 10^{11} photons per pulse, X-ray spot size focused down to 100×100 nm², a value of P equal to 25 needed to satisfy the Rose criterion.

	Nuclear energy-related materials						Reactor coolants		Waste disposals clay
	Materials of current and future advanced nuclear reactors						Coolant/nanofluid		barrier
	Fuel/structure/moderator								Na-mont morillonite ^a
	Uranium dioxide, UO ₂	ODS steel PM2000 ^a	Zirconium, Zr	Silicon carbide, SiC	Graphite, C		Water, H ₂ O	Alumina, Al ₂ O ₃	
Spatial resolution d (nm)	1.5	1.7	1.8	2.4	2.4		4.1	2.1	2.8

^a The chemical formula of the PM2000 steel (oxide dispersion strengthened (ODS) steel) and of the Na-montmorillonite clay are $\text{Fe}_{0.745}\text{Cr}_{0.19}\text{Al}_{0.055}\text{Ti}_{0.005}(\text{Y}_2\text{O}_3)_{0.005}$ and $[(\text{Si}_{3.96}\text{Al}_{0.04}\text{O}_{10})(\text{OH})_2](\text{Al}_{1.52}\text{Fe}_{0.18}\text{Mg}_{0.27})\text{Na}_{0.4}$, respectively. The refractive index (δ) and the absorption index (β) have been obtained from [17].

transverse, or spatial, coherence, the longitudinal or temporal coherence, which is inversely proportional to the photon bandwidth, is quite poor. Although this can be improved by monochromatization or by seeding, poor longitudinal coherence limits the resolution achievable, particularly in thick samples. Finally, it is attractive to consider time-resolved pump–probe measurements of coherent scattering at the X-ray FEL. Since the sample will in general be destroyed, only a single-shot will be available to image a particular region of the sample; it is not possible to increase the resolution by accumulating speckle patterns from successive shots or to simply take repeat shots with different time delays to produce a “molecular movie”. It is thus predicted that coherent imaging of nuclear energy-related materials will be limited in resolution to 2 nm as mentioned above (Table 2), and dynamic effects must be sampled in a statistical manner. It will generally be necessary to assume a physical model for the process under study and to compare predictions of the resulting spatial and temporal correlation functions with those extracted from the scattering data. While individual scattering patterns cannot be accumulated, this is not true for the extracted correlations.

2.3.3. X-ray photon correlation spectroscopy

In principle, the dynamics of a fluctuating system in equilibrium can be observed with coherent X-rays simply by comparing succes-

sive speckle patterns recorded as a function of time. This technique is known in optics as dynamic light scattering and with X-rays as X-ray photon correlation spectroscopy (XPCS). Of course, the advantages of X-rays are a finer spatial resolution and elemental contrast. The advent of X-ray FEL radiation offers further the great advantages of high spatial coherence and sub-ps time resolution. A major difficulty in achieving this time resolution, however, arises from the relatively slow frame rate possible with imaging detectors, typically 100 Hz. A solution to the frame-rate problem is the so-called “split-pulse” XPCS method [20] (see Fig. 5), where the incoming X-ray FEL pulse is split and delayed, to produce two equal-intensity X-ray FEL pulses with a variable time delay τ , and where the detector thus registers a double-exposure speckle pattern [21].

By means of such an XPCS experiment, the time correlations of the coherently scattered radiation intensity from a fluctuating sample can be quantified via the intensity autocorrelation function $g_2(\tau) = \langle I(t) \times I(t + \tau) / \langle I(t) \rangle^2 \rangle$, where $I(t)$ represents the scattering intensity detected at time t .

In case of Gaussian fluctuations, $g_2(\tau)$ is given by $g_2(\tau) = 1 + |S(q, \tau)|^2$ [22], where $S(q, \tau)$ represents the so-called “intermediate scattering function”. $S(q, \tau)$, is obtained by measuring the contrast as a function of time delay τ between two consecutive X-ray FEL pulses and scattering angle θ . It describes the temporal and spatial

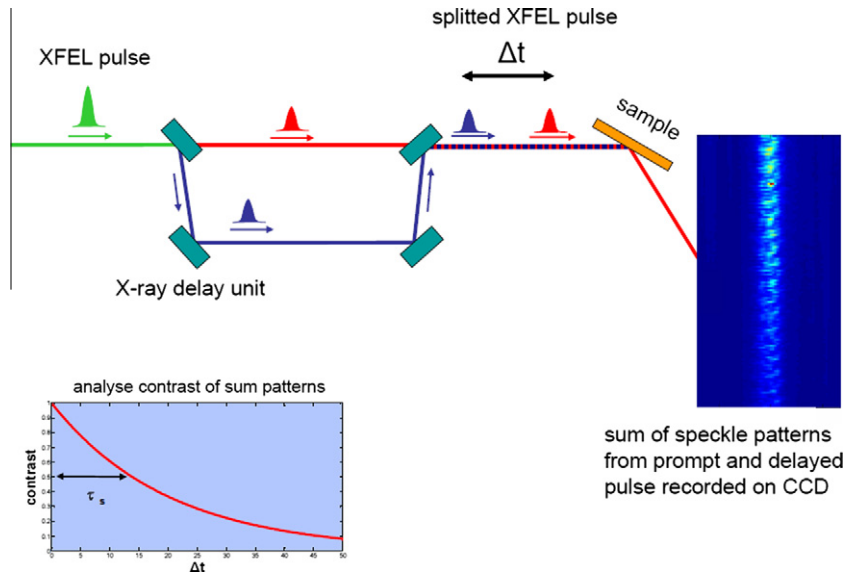


Fig. 5. A conceptual split-and-delay XPCS experiment, in which two copies of an X-ray FEL pulse, separated in time by τ (τ correspond to Δt in Fig. 5) scatter on the sample (yellow) to produce a double-exposure speckle pattern at the detector. Measuring the resulting speckle contrast as a function of the time delay τ and the scattering angle θ yields the intermediate scattering function $S(q, \tau)$. The correlation times of the system (τ_s) can then be measured [20]. Reprinted from [20]. Copyright (2007), with the permission of Elsevier. (For interpretation of the references to colour in this figure legend, the reader is referred to the web version of this article.)

evolutions of the intensity correlations in the fluctuating sample which can be directly compared with model calculations. Indeed, the dynamical changes of the sample on the time scale of the two pulses will lead to a change in the contrast of the speckle pattern recorded during this double-exposure probe–probe XPCS measurement. If τ is much shorter than the typical sample correlation time τ_c , a sharply-defined, high-contrast speckle pattern will be observed. If, on the other hand, τ is long compared to τ_c , a low-contrast pattern will result. Note that τ_c depends not only on sample conditions such as concentration and temperature, but that it will also show a dependence on the wave-vector q , via the scattering angle θ . Indeed, the wave-vector q is related to the scattering angle θ as follows: $q = (4\pi \times \sin \theta) / \lambda$. At small scattering angle (i.e. small q), one is predominantly sensitive to long-wavelength fluctuations, and vice versa. Using “split-pulse” XPCS, correlation times on time scale down to the minimum duration of the X-ray FEL pulse can typically be measured. Indeed, the positions of the optical components within the X-ray delay line govern the beam path between the two delayed X-ray FEL pulses, and *a fortiori* the time delay τ between the two split X-ray FEL pulses. A pulse splitter with a 3×10^{-4} m path length would thus lead to a 10^{-12} s time delay τ . Thanks to the development of the X-ray delay line for “split-pulse” XPCS measurements, the pulse duration of the X-ray FEL pulse represents the limiting factor for the temporal resolution, and it is expected that ~ 20 -fs correlation times could be measured at the SwissFEL facility.

In the “kinematical” or “single scattering” approximation, a quantitative estimate of the scattering intensity, I_{sc} , can be obtained from the mathematical equation describing the intensity of a X-ray FEL pulse scattered by the electrons which composed a given type of atom. The scattering intensity, I_{sc} , is given by:

$$I_{sc} = \frac{I_0}{A_0} \times \Delta\Omega \times r_e^2 \times |f^0(\sin \theta / \lambda)|^2 \times N_{atom} \quad (4)$$

where

$$f^0(\sin \theta / \lambda) = \sum_{i=1}^4 a_i \times \exp(-b_i \times (\sin \theta / \lambda)^2) + c \quad (5)$$

(for $0 < \sin \theta / \lambda < 2.0 \text{ \AA}^{-1}$)

is known as the atomic scattering factor. The atomic scattering factor represents a measure of the scattering amplitude of the X-rays by an isolated atom. Based on the nine Cromer–Mann coefficients a_i , b_i , and c (with $i = 1, \dots, 4$) of the atomic scattering factor, which can be computed for a given atom [23], and on the X-ray wavelength λ , the scattering intensity per pixel and per pulse can be estimated by considering the incident beam intensity I_0 , the cross-sectional area of the scattered beam A_0 , the detector view angle for accepting the photons $\Delta\Omega$, the classical electron radius r_e (Eq. (1)), and the number of atoms of a given type involved in the scattering process, N_{atom} . It has recently been shown that at a level of only 0.1 photons per pixel, useful contrast information can still be extracted from simulated double-exposure speckle pattern obtained from “split-pulse” XPCS [24]. Westermeier et al. [25] have also reported the low average number of photons per pixel and per accumulation time – i.e. a number of less than one – which can be successfully achieved by using the single-photon-counting PILATUS detector.

A stringent requirement in split-pulse XPCS at an X-ray FEL large facility is that the first of the two X-ray FEL pulses does not significantly perturb the sample. In spite of the heavy intensity losses inherent in a practical split-and-delay unit, this will certainly require the use of unfocused radiation and probably of an additional beam attenuator. Note again, however, that the correlation data $S(q, \tau)$ can be accumulated over many shots, thereby improving the statistical accuracy.

3. Proposed tests of nuclear materials simulations using X-ray FEL

3.1. Nucleate boiling heat transfer in reactor systems

Boiling remains one of the most effective mechanisms for heat transfer from a hot surface to a cooling liquid. A better understanding of the fundamental phenomena underlying boiling heat transfer would improve our current capabilities for addressing nuclear reactor safety issues. However, a comprehensive fundamental understanding of the relevant phenomena occurring at the atomic length scale and affecting the dynamics of the boiling of water has only been partially achieved.

To date, main achievements at the atomic level arise from numerical approaches of the nucleate boiling primary processes [26]. Insight into a better understanding of the boiling of water at the atomic level has been achieved from molecular dynamics simulations of liquid–vapor interface in liquid water [27] (see Fig. 6). Indeed, Fig. 6 nicely shows the early stages of the boiling processes and especially the dynamical evolution of single and/or groups of water molecules, and of small vacuum cavities in liquid water.

The study of the course of the boiling of water at metallic surfaces has also received attention. Interestingly, neutron irradiated stainless steel rods [28] exhibit enhanced heat flux, this enhancement in the heat flux being often attributed to the higher wettability of the irradiated materials. Surface properties have been long recognized as one of the important factors influencing boiling, but how their variation affects the dynamic of the liquid–vapor interface close to the material surface is unclear. Furthermore, how this higher wettability translates into a higher heat flux remains uncertain. Based on the pioneer work of Wayner et al. [29] on evaporating wetting films, Dhir and co-workers [30] developed a simple model to calculate the evaporative heat flux through a tiny region at the contact region of liquid–vapor interface with the solid surface, but the accuracy of this model has not been proven yet.

Under this situation, development of appropriate experiments in terms of temporal and spatial resolution is needed. We thus propose to investigate the homogeneous and heterogeneous bubble nucleation by triggering the nucleation of the vapor phase by laser-induced local heating of water, and by following the course of the boiling process by coherent X-ray scattering. Sub-ns boiling processes of isopropanol liquid films in contact with a laser-heated silicon wafers have been investigated by optical measurements [31]. Improvements in the spatial and the temporal resolutions have recently been achieved from time-resolved X-ray diffuse scattering investigations of phase transitions in superheated liquid [32]. Extending this analytical approach to coherent scattering measurements at an X-ray FEL should potentially enable near-atomic-scale measurements of the three-dimensional shape and the sub-ps dynamics of the liquid–vapor interface.

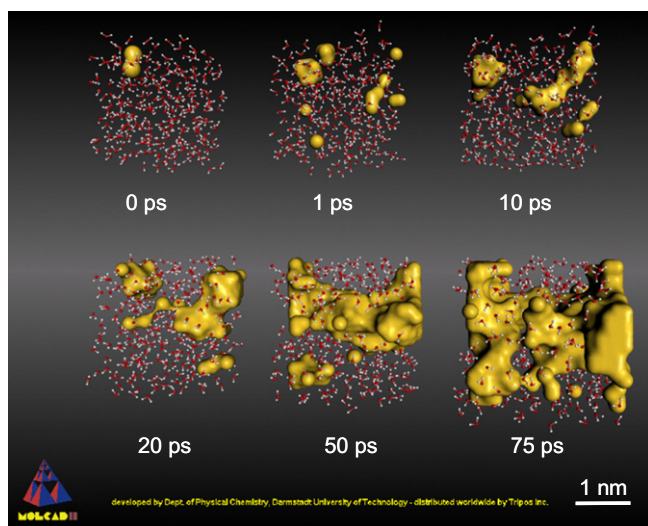


Fig. 6. Sequence of snapshots obtained from molecular dynamics simulations showing the course of the boiling of water [27]. The shape and size of the cavity regions (in yellow) in liquid water change dramatically in the course of time propagation. Reprinted figure with permission from [27]. Copyright (2004) by the American Physical Society. (For interpretation of the references to colour in this figure legend, the reader is referred to the web version of this article.)

Another issue concerns the effect of nanofluid on the boiling heat transfer and on the thermal crises (e.g. critical heat transfer). Some advanced Generation III + light water reactors (e.g. AP1000, APR1400) during postulated severe accident rely on the in-vessel retention strategy, which consists in flooding the Reactor Pressure Vessel (RPV) cavity with water so that the cooling can be assured and RPV failure avoided. Research investigations [33] pointed out that by injecting colloidal dispersions of nanoparticles (e.g. Al_2O_3 , as nanofluid materials with size in the range 1–100 nm and concentration close to 0.001 vol.%) into water, the heat removed during boiling will be enhanced, increasing the level at which critical heat flux would occur. It should be pointed out, that currently in the in-vessel retention strategy, it is not foreseen to use nanofluid, because the effect on the thermal crises is not yet well understood. In this context, it is proposed to investigate nanofluid deposition on metallic plates as a function of several parameters, e.g. type of nanofluid, concentration, size, type of metallic plate and surface characteristics. Coherent X-ray scattering has already proven to be a very suitable technique for three-dimensional structural determination of a biological system from a single-shot 2D diffraction pattern [34] and for the morphological determination of carbonaceous nanoparticles [35]. Such results lend strong support to the application of coherent X-ray scattering at hard X-ray FELs in resolving the 3D structure and morphology of such nanofluids.

3.2. Radiation-induced displacement cascades and crack propagation in nuclear reactors materials

The radiation tolerance of structural materials in fission nuclear reactors is an important issue for the safe operation of current and future advanced nuclear plants. Upon particle irradiation, irradiation-induced primary defects (interstitial and vacancy) [36] can form in nuclear reactor materials such as fuel claddings (Zr-alloys), (advanced) reactor pressure vessel steels, ceramics, composite materials, and the graphite used in high temperature reactors (HTR). The molecular dynamics simulation method represents a powerful method for the investigation of the time evolution of these defect structures. Several relevant examples of the application of this simulation method are reported in the literature [37–43]. Fig. 7 presents results from molecular dynamics simulations of a 5 keV displacement cascade in a 12 nm grain in nanocrystalline Ni [41].

Experimental verification of the dynamical behavior of such processes related to irradiation-induced phenomena is needed. A «pump–probe» coherent scattering experimental scheme is thus proposed: the process could be triggered by a synchronized high-energy particle ion-implanter (the pump), the probe consisting of diffuse scattering of the X-ray FEL pulse. Such an experimental methodology would determine statistical features of the crystallographic development of irradiation cascades directly after their initiation. The statistical nature of the formation of the primary interstitial and vacancy defects and their nanometer-sized clusters leading to dislocation loops, and precipitates, as well as the evolution of their structure, distribution, and mobility, should in principle be accessible on a time scale in the range ~ 0.1 –100 ps. The average size and density of the central vacancy cluster and the diffusion rate of the vacancies and interstitials clusters should be obtained through correlation analysis of scattering. A spatial resolution of ~ 2 nm is estimated to be achieved from X-ray scattering experiments on different relevant nuclear reactor materials (Table 2). Such experimental results will then be compared to molecular dynamics simulations, allowing the experimental validation of the simulations [6], as well as a better understanding of the materials' resistance to particle irradiation [43].

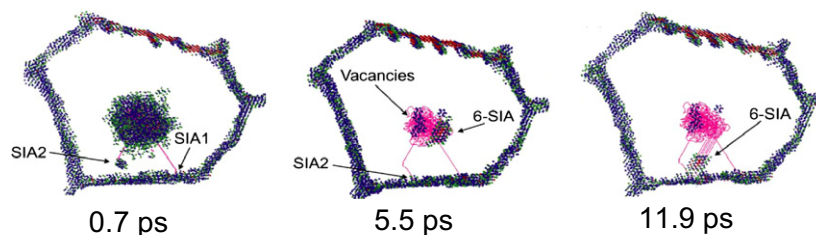


Fig. 7. Results from molecular dynamics simulations showing the development of the cascade of the primary damage state in a 12 nm grain in nanocrystalline Ni (time scale: 0.7–11.9 ps, length scale: ~ 10 nm). SIA refers to self-interstitial atoms (taken from [41]). Reprinted from [41]. Copyright (2003), with permission from Elsevier. The length and time scales accessible via molecular dynamics simulations fit particularly well those accessible with the SwissFEL [44].

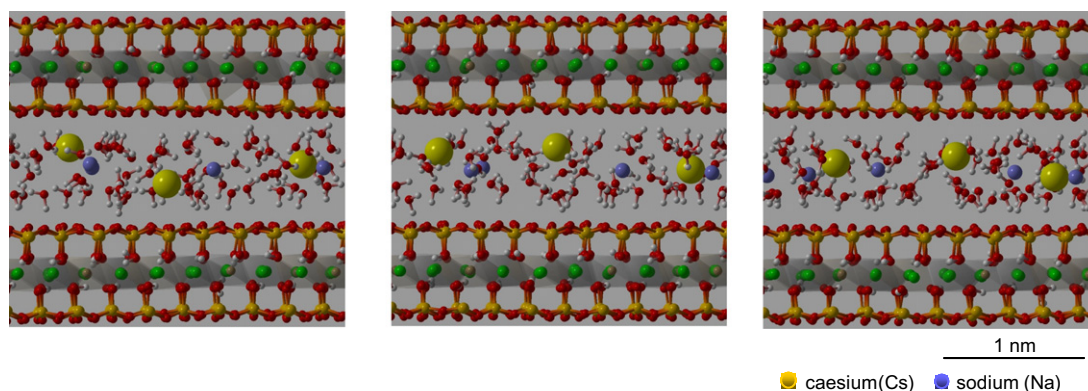


Fig. 8. Sequence of snapshots, from left to right, of a molecular dynamics simulation for bi-hydrated montmorillonite, showing the propagation of Na (blue spheres), Cs (yellow spheres) and H_2O molecules (oxygen atoms are red and hydrogen atoms are gray) in the interlayer, at time intervals of 10 ps. Clay particles (montmorillonite) consist of a layer of Al octahedra (shown as gray with a green sphere in the center) sandwiched between two silicon tetrahedral layers (Si atoms are light brown). (For interpretation of the references to colour in this figure legend, the reader is referred to the web version of this article.)

Further crucial knowledge for the integrity assessment of reactor pressure vessel steels could also be gained by investigating the deformation mechanisms underlying the ductile-to-brittle transition of ferritic/martensitic steels upon loading conditions [45]. Previous work demonstrating laser-induced crack initiation on the ns scale in brittle materials and describing the complexity of the resulting crack networks is reported in the literature [46]. Thanks to this already-implemented pump laser technique, proposal is made to conduct «pump–probe» coherent scattering experiments on reactor pressure vessel steels; a laser-induced shock wave (the pump) could be used to trigger the deformation process of the materials, while the probe would consist of the diffuse scattering of the X-ray FEL pulse. Such X-ray FEL based investigations will plausibly provide statistical properties of the crack initiation and propagation, and of the dislocations network around the crack tip, and a fortiori a stringent test of the method and of the parameters used in simulations of crack propagation [47]. Indeed, the length and time scales of such computer simulations fit very well to the spatial and temporal scales accessible with X-ray FEL-based experiments.

3.3. Ion diffusion in clay minerals

Thanks to the low hydraulic conductivity, clay rich rocks are used as barriers for environmental protection of radioactive and toxic waste disposals. Slow migration of pollutants in engineered barriers arises from stochastic motion of cations in the interlayer of clay minerals. In-depth understanding of the ion diffusion processes in the interlayer of clay minerals, which size is on the order of 1 nm is indispensable for long term environmental safety assessments of waste disposals. To date, such processes which occur at

time scales ranging from ~ 10 – 100 ps are accessible via molecular dynamics simulations [48]. An example of molecular dynamics simulations showing the propagation of the Na, Cs and H_2O molecular species in the interlayer of a montmorillonite clay system are presented in Fig. 8.

Such calculations need to be experimentally verified. The Brownian motion of ions in the inter-particle and interlayer space of clay minerals is here thus proposed to be investigated by performing split-pulse XPCS measurements of q -dependence correlation times [20], for X-ray FEL pulses separated in time by 10 ps. The ability of synchrotron-based measurements to obtain a quantitative understanding of the dynamics of disorder in alloys has already been reported in the literature [49,50]. From their work, Leitner et al. have been able to probe the so far inaccessible atomic-scale diffusion parameter such as the bulk diffusivity of a single atom in a short-range ordered single crystal $\text{Cu}_{90}\text{Au}_{10}$ alloy, proving the ability of the XPCS technique to study dynamics of disorder in well-ordered materials. Such results lend strong support to XPCS at the X-ray FEL to quantify the mobility of the interlayer molecular species in clay minerals at ps and even sub-ps time scales. It is estimated that a single X-ray FEL pulse (containing 10^{11} hard X-ray photons – with a X-ray energy $h\nu$ of 12.4 keV (i.e. a X-ray wavelength λ of 1 Å) – focused into a $100 \times 100 \text{ nm}^2$ spot, will yield a resolution of approximately 3 nm (Table 2). Under such experimental conditions, the scattering intensity, by $\sim 10^{28}$ Cs atoms located in a montmorillonite sample, of an X-ray FEL pulse with 10^{11} photons at an energy of 12.4 keV focused down to $100 \times 100 \text{ nm}^2$, is predicted to be close to 1 scattered photon per pixel, for small values of scattering angles θ in the range 0 – 2° (see Eqs. (4) and (5)); such a number of detected scattered photons being probably compatible with the high performances of the

PILATUS detector [25]. Note that these calculations are done for a 10- μm thick montmorillonite sample and a Cs concentration of 1.25 Cs atoms. nm^{-3} . A better understanding of the dependence of atomistic quantities such as e.g. diffusion activation energies on the local atomic structure could thus be gained by taking advantage of the full coherence of the XFEL radiation. Furthermore, such novel quantitative information on the diffusion mobility of the interlayer species in clay materials will serve as experimental input to assist the development of robust geochemical databases on diffusion processes in clay systems for performance assessments of the clay barrier in the deep geological disposal of radioactive waste.

3.4. Chemical structure of graphite dust aerosol and colloidal clay particles

Clay colloidal particles could play an important role in contaminant transport in natural groundwater systems. The dynamic behavior of clay colloids in groundwater is related to the structural

and chemical properties of their constituents. Characterization of the structure of these clay colloid aggregates is of fundamental importance in order to gain knowledge about their sedimentation behavior and their colloid contaminant transport properties in natural systems. Scanning transmission X-ray microscopy (STXM) measurements revealed that montmorillonite colloid aggregates have spherical and occasionally ellipsoidal shapes and sizes of order 100–800 nm [51]. Such colloid aggregates are shown in Fig. 9.

Also, graphite dust represents one of the most important issues for the safety of HTRs. Dust is generated in HTRs by several mechanisms, one of the most significant ones being the abrasion when graphite parts move relative to one another, or to metal parts in the reactor, or by abrasion by high gas velocities. The generated dust may become contaminated by the leakage of radioactive compounds, e.g., Ag, Cs, Sr, I, from the fuel particles [52]. During operation, the generated dust is accumulated in the reactor core, as well as in the steam generator/heat exchange system. The accumulated dust may be released if the flow is suddenly increased, e.g. due to a fast depressurization following a breach of the primary system pressure boundary. Subsequently, the activity contained in the dust particles, as the major transport vehicle for the activity transport, will be released from the primary system [53]. For the development of HTR technology, it is of critical importance to characterize the graphite dust for its structure and particle size distribution, as well as for its ability to adsorb radioactive compounds.

The proposal is made to perform an elemental and structural analysis of the fraction of graphite dust particles and clay colloid aggregates having a nanometer size by performing single-pulse resonant coherent X-ray diffraction for elemental specificity. Resonant coherent imaging is foreseen to be combined with single-shot spectroscopic measurements to gain insight into the chemical structure at the molecular level which govern the sorption of radioactive species on these particles. Methods developed for aerosol mass spectrometer inlets (e.g. [54]) can be applied to overcome the challenge of injecting single particles into the X-ray

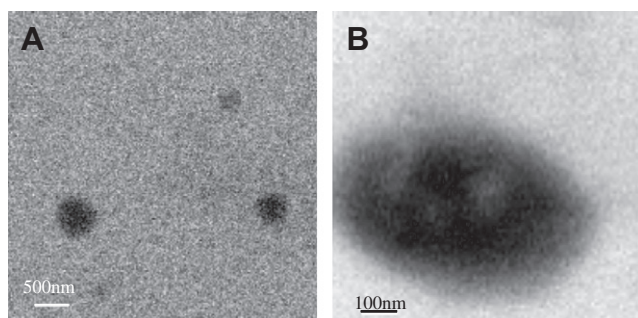


Fig. 9. STXM images of (a) colloidal clay aggregates, and a zoom view of (b) an individual colloidal clay aggregate (Adapted from [51]). Reprinted from [51]. Copyright (2009) with the permission of Elsevier.

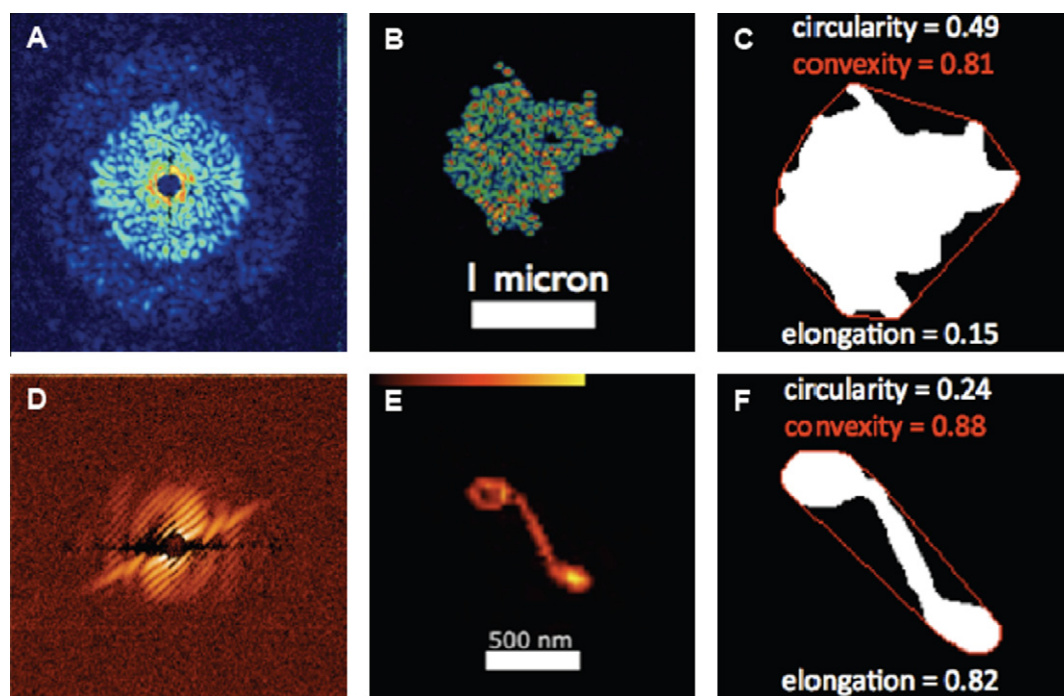


Fig. 10. In situ coherent diffraction measurements performed on carbonaceous nanoparticles at the FLASH soft X-ray free electron laser ($\lambda = 7$ nm, achieved resolution = 35 nm) [35]. "Aerosol Science & Technology: Aerosol imaging with a soft X-ray Free Electron Laser", (44): i–vi. Copyright 2010. Mount Laurel, NJ. Reprinted with permission.

beam. Since disturbances to particles may occur upon mounting prior to measurements, aerosol injection at FELs is less destructive and thus preferred [35]. The ability of the coherent diffraction technique to image crystalline and non-crystalline samples on the nanometer scale has been reported in the literature [33,55–59]. An example of application of this technique in aerosol science and technology is presented in Fig. 10. The morphology of fibrous and aggregated spherical carbonaceous nanoparticles has been determined with a 35 nm resolution.

Coherent X-ray diffraction at the shorter X-ray wavelengths to be delivered by hard X-ray FEL facilities will give improved resolution: from the dose-resolution relation given in [16], it can be estimated that a single X-ray FEL shot will yield a resolution of approximately 2 nm (Table 2). The combination of the use of short X-ray wavelengths with the tuning of the photon wavelength to specific absorption resonances would bring the advantage of elemental specificity at a nm-scale resolution. The advantage of using X-ray FEL in the present cases is that it will circumvent the problem of radiation damage via the “diffract-and-destroy” mode.

4. Conclusions

The source performance delivered by an X-ray free electron laser, and in particular by the proposed SwissFEL facility, opens new horizons in many areas of scientific research, including that of nuclear materials science and technology. In this paper, several categories of pertinent scientific questions related to nuclear energy research are presented. Such scientific questions require the capabilities of single-shot X-ray spectroscopy, coherent X-ray scattering and/or X-ray photon correlation spectroscopy, to be provided by the X-ray FEL. Potential progress in nuclear materials science, radionuclide geochemistry, and thermal hydraulics of reactors are anticipated. A direct benefit of such proposed X-ray FEL investigations at the nm and ps length and time scales will be the confirmation and refinement of the numerical simulation techniques and parameters presently in use. Further X-ray FEL applications in the field of nuclear materials science and technology will surely follow.

Acknowledgments

The authors wish to thank M. Andreani, J. Chen, E. Curti, K. Foskolos, W. Hoffelner, K. Janssens, G. Kuri, M. Martin, B. Niceno, M. Niffenegger, D. Popov, S. Portier, M.A. Pouchon, H.-M. Prasser, M. Samaras, H.-P. Seifert, S. Valance, E. Wieland, as well as R. Abela, H.-H. Braun, A. Cervellino, F. Gozzo, D. Grolimund, G. Ingold, S. Johnson, B. Pedrini and M. van Daalen from the SLS and the SwissFEL teams for helpful discussions and interest in the work. J.A. van Bokhoven, F. van der Veen, G. Grübel, D. Zahn, M. Samaras, M.J. Bogan are also thanked for accepting to provide support materials already published elsewhere and reused in this manuscript.

References

- [1] E.L. Saldin, E.A. Schneidmiller, M.V. Yurkov, *The Physics of Free Electron Lasers*, Springer, Berlin, Germany, 1999.
- [2] B.D. Patterson (Ed.), *Ultrafast Phenomena at the Nanoscale: Science Opportunities at the SwissFEL X-Ray Laser*, PSI Report Nr. 09-10, 2009.
- [3] https://slacportal.slac.stanford.edu/sites/lcls_public/Pages/Default.aspx.
- [4] M. Altarelli et al. (Ed.), *The European X-Ray Free-Electron Laser, Technical Design Report*, Hamburg, Germany, 2006. ISBN: 978-3-935702-17-1.
- [5] T. Tanaka, T. Shintake (Eds.), *SCSS XFEL Conceptual Design Report*, 2005.
- [6] B.D. Patterson, R. Abela, H.-H. Braun, U. Flechsig, R. Ganter, Y. Kim, E. Kirk, A. Oppelt, M. Pedrozzi, S. Reiche, L. Rivkin, Th. Schmidt, B. Schmitt, V.N. Strocov, S. Tsujino, A.F. Wrulich, *New J. Phys.* 12 (2010) 035012.
- [7] L.X. Chen, *Angew. Chem. Int. Ed.* 43 (2004) 2886–2905.
- [8] C. Bressler, C. Milne, V.-T. Pham, A. ElNahas, R.M. van der Veen, W. Gawelda, S. Johnson, P. Beaud, D. Grolimund, M. Kaiser, C.N. Borca, G. Ingold, R. Abela, M. Chergui, *Science* 323 (2009) 489–492.
- [9] M. Chergui, *Acta Cryst. A66* (2010) 229–239.
- [10] O.V. Safonova, M. Tromp, J.A. van Bokhoven, F.M.F. de Groot, J. Evans, P. Glatzel, *J. Phys. Chem. B* 110 (2006) 16162–16164.
- [11] S. Pascarelli, O. Mathon, M. Muñoz, T. Mairs, J. Susini, *J. Synchrotr. Rad.* 13 (2006) 351–358.
- [12] C.G. Ryan, D.P. Siddons, G. Moorhead, R. Kirkham, P.A. Dunn, A. Dragone, G. De Geronimo, *Nucl. Instr. and Meth. in Phys. Res. B* 260 (2007) 1–7.
- [13] V.N. Strocov, *J. Synchrotr. Rad.* 17 (2010) 103–106.
- [14] H.S. Isaacs, P. Schmuki, S. Virtanen, in: D.R. Baer, C.R. Clayton, G.P. Halada, G.D. Davis (Eds.), *State of the Art Application of Surface and Interface Analysis Methods to Environmental Material Interactions*, 2001.
- [15] F. van der Veen, F. Pfeiffer, *J. Phys.: Condens. Matter* 16 (2004) 5003–5030.
- [16] M.R. Howells, T. Beetz, H.N. Chapman, C. Cui, J.M. Holton, C.J. Jacobsen, J. Kirz, E. Lima, S. Marchesini, H. Miao, D. Sayre, D.A. Shapiro, J.C.H. Spence, D. Starodub, *J. Electron Spectrosc. Relat. Phenom.* 170 (2009) 4–12.
- [17] http://henke.lbl.gov/optical_constants/getdb2.html.
- [18] C. Song, R. Bergstrom, D. Ramunno-Johnson, H. Jiang, D. Paterson, M.D. de Jonge, I. McNulty, J. Lee, K.L. Wang, J. Miao, *Phys. Rev. Lett.* 100 (2008) 025504.
- [19] R. Neutze, R. Wouts, D. van der Spoel, E. Weckert, J. Hadju, *Nature* 406 (2000) 752–757.
- [20] G. Grübel, G.B. Stephenson, C. Gutt, H. Sinn, Th. Tschentscher, *Nucl. Instr. and Meth. in Phys. Res. B* 262 (2007) 357–367.
- [21] G. Grübel, C. Schüssler-Langeheine, C. Gutt, P. Wochner, B. Stephenson, B. Sepiol, A. Madsen, M. Yurkov, Report of the Working Group II on X-ray Photon Correlation Spectroscopy, in: *International Workshop on the Materials Imaging and Dynamics Instrument at the European XFEL*, European Synchrotron Radiation Facility (ESRF), Grenoble, France, October 28–29, 2009.
- [22] C. Gutt, L.M. Stadler, A. Duri, T. Autenrieth, O. Leupold, Y. Chushkin, G. Grübel, *Opt. Exp.* 17 (2009) 55–61.
- [23] D.T. Cromer, J.B. Mann, *Acta Cryst. A* 24 (1968) 321–324.
- [24] B.D. Patterson, R. Abela, Th. Feurer, U. Flechsig, M. Kläui, B. Pedrini, M. Shalaby, M. van Daalen, *PSI Scientific Report*, 2009, pp. 8–9. ISSN: 1662-1719.
- [25] F. Westermeier, T. Autenrieth, C. Gutt, O. Leupold, A. Duri, A. Menzel, I. Johnson, C. Broennimann, G. Grübel, *J. Synchrotr. Rad.* 16 (2009) 687–689.
- [26] V.V. Yagov, *Heat Mass Transf.* 45 (2009) 881–892.
- [27] D. Zahn, *Phys. Rev. Lett.* 93 (2004) 227801.
- [28] Y. Sibamoto, T. Yonamoto, H. Nakamura, Y. Kukita, *J. Nucl. Sci. Technol.* 44 (2007) 183–193.
- [29] P.C. Wayner Jr., Y.K. Kao, L.V. LaCroix, *Int. J. Heat Mass Transfer* 19 (1976) 487–492.
- [30] J.H. Lay, V.K. Dhir, *J. Heat Transfer* 117 (1995) 394–401.
- [31] F. Lang, P. Leiderer, *New J. Phys.* 8 (2006) 14.
- [32] A.M. Lindenberg, S. Engemann, K.J. Gaffney, K. Sokolowski-Tinten, J. Larsson, P.B. Hillyard, D.A. Reis, D.M. Fritz, J. Arthur, R.A. Akre, M.J. George, A. Deb, P.H. Bucksbaum, J. Hajdu, D.A. Meyer, M. Nicoul, C. Blome, Th. Tschentscher, A.L. Cavalieri, R.W. Falcone, S.H. Lee, R. Pahl, J. Rudati, P.H. Fuoss, A.J. Nelson, P. Krejčík, D.P. Siddons, P. Lorazo, J.B. Hastings, *Phys. Rev. Lett.* 100 (2008) 135502.
- [33] J. Buongiorno, L.W. Hu, G. Apostolakis, R. Hannink, T. Lucas, A. Chupin, *Nucl. Eng. Des.* 239 (2009) 941–948.
- [34] K.S. Raines, S. Salha, R.L. Sandberg, H. Jiang, J.A. Rodriguez, B.P. Fahimian, H.C. Kapteyn, J. Du, J. Miao, *Nature* 463 (2010) 214–217.
- [35] M.J. Bogan, S. Boutet, H.N. Chapman, S. Marchesini, A. Barty, W.H. Benner, U. Rohner, M. Frank, S.P. Hau-Riege, S. Bajt, B. Woods, M.M. Seibert, B. Iwan, N. Timneanu, J. Hajdu, J. Schulz, *Aerosol Sci. Technol.* 44 (2010) i–vi.
- [36] H. Ullmaier, W. Schilling, *Radiation damage in metallic reactor materials*, in: *Physics of Modern Materials*, Vol. I, International Atomic Energy Agency, Vienna, 1980.
- [37] W.J. Phythian, R.E. Stoller, A.J.E. Foreman, A.F. Calder, D.J. Bacon, *J. Nucl. Mater.* 223 (1995) 245–261.
- [38] J.M. Delaye, D. Ghaleb, *J. Nucl. Mater.* 244 (1997) 22–28.
- [39] R.E. Stoller, *J. Nucl. Mater.* 276 (2000) 22–32.
- [40] Y.N. Osetsky, D.J. Bacon, B.N. Singh, B. Wirth, *J. Nucl. Mater.* 307–311 (2002) 852–861.
- [41] M. Samaras, P.M. Derlet, H. van Swygenhoven, M. Victoria, *J. Nucl. Mater.* 323 (2003) 213–219.
- [42] D.J. Bacon, Y.N. Osetsky, R. Stoller, R.E. Voskoboinikov, *J. Nucl. Mater.* 323 (2003) 152–162.
- [43] B.D. Wirth, *Science* 318 (2007) 923–924.
- [44] B.D. Wirth, G.R. Odette, J. Marian, L. Ventelon, J.A. Young-Vandersall, L.A. Zepeda-Ruiz, *J. Nucl. Mater.* 329–333 (2004) 103–111.
- [45] G.R. Odette, G.E. Lucas, *JOM* 53 (2001) 18–22.
- [46] X.-Z. Li, M. Nakano, Y. Yamauchi, K. Kishida, *J. Appl. Phys.* 83 (1998) 3583–3594.
- [47] D. Farkas, S. van Petegem, P.M. Derlet, H. van Swygenhoven, *Acta Mater.* 53 (2005) 3115–3123.
- [48] G. Kosakowski, S.V. Churakov, T. Thoenen, *Clays Clay Miner.* 56 (2008) 190–206.
- [49] M. Leitner, B. Sepiol, L.-M. Stadler, B. Pfau, G. Vogl, *Nat. Mater.* 8 (2009) 717–720.
- [50] S. Brauer, G.B. Stephenson, M. Sutton, R. Brüning, E. Dufresne, S.G.J. Mochrie, G. Grübel, J. Als-Nielsen, D.L. Abernathy, *Phys. Rev. Lett.* 74 (1995) 2010–2013.
- [51] C. Degueldre, J. Raabe, S. Wold, *Appl. Geochem.* 24 (2009) 2015–2018.
- [52] R. Moormann, *Science and Technology Of Nuclear Installations*, Hindawi Publishing Corporation (2008) Article ID 597491, 14 pp. doi:1155/2008/597491.

- [53] M.P. Kissane, Nucl. Eng. Des. 239 (2009) 3076–3091.
- [54] M.V. Johnston, J. Mass Spectrom. 35 (2000) 585–595.
- [55] R. Neutze, R. Wouts, D. van der Spoel, E. Weckert, J. Hadju, Nature 406 (2000) 752–757.
- [56] J. Miao, P. Charalambous, J. Kirz, D. Sayre, Nature 400 (1999) 342–344.
- [57] H.N. Chapman, A. Barty, M.J. Bogan, S. Boutet, M. Frank, S.P. Hau-Riege, S. Marchesini, B.W. Woods, S. Bajt, W.H. Benner, R.A. London, E. Plönjes, M. Kuhlmann, R. Treusch, S. Düsterer, T. Tschentscher, J.R. Schneider, E. Spiller, T. Möller, C. Bostedt, M. Hoener, D.A. Shapiro, K.O. Hodgson, D. van der Spoel, F. Burmeister, M. Bergh, C. Caleman, G. Huldt, M.M. Seibert, F.R.N.C. Maia, R.W. Lee, A. Szöke, N. Timneanu, J. Hadju, Nat. Phys. 2 (2006) 839–843.
- [58] R. Treusch, J. Feldhaus, New J. Phys. 12 (2010) 035015.
- [59] J. Miao J, T. Ishikawa, Q. Shen, T. Earnest, Annu. Rev. Phys. Chem. 59 (2008) 387–410.